

AE 370 Group Project 2 : Axial Vibration of a Nonuniform Rod

Eric Chiang, Jonah Wu, Josué R. Bashombe

University of Illinois at Urbana-Champaign

Department of Aerospace Engineering

1 Introduction

In this project, we investigate an engineering-relevant initial-boundary value problem (IBVP) through the lens of numerical analysis. Working collaboratively in a small group, we selected a physically meaningful problem, developed a mathematical formulation, and implemented a numerical method suitable for its solution. Our goal is to explore both the theoretical and computational aspects of the problem while uncovering behaviors that are of practical interest in engineering applications.

The focus of this report is to document our modeling approach, justify the numerical techniques employed, and present the results of a series of systematic studies designed to answer meaningful questions about the dynamics governed by the IBVP. Emphasis is placed not only on correctness and clarity of the numerical implementation, but also on interpreting the physical implications of the results and assessing the sensitivity of the solution to changes in key parameters.

This document is structured to reflect the key evaluation criteria, including problem formulation, method development, validation, and analysis. Through this project, we aim to deepen our understanding of partial differential equations in engineering contexts and gain insight into how numerical simulations can illuminate real-world behavior.

2 Problem Selection and Formulation

In this section, we present the initial-boundary value problem (IBVP) selected for our study. Our goal was to identify a problem that is both relevant to real-world engineering applications and suitably complex to allow for meaningful exploration, while remaining numerically tractable.

After considering various options, we selected the axial vibration of a nonuniform rod. This problem introduces spatial variation in material properties—an important consideration in the design and analysis of aerospace structures, robotic components, and other mechanical systems. The IBVP is linear and one-dimensional, but its non-constant coefficients make it rich in behavior and well-suited for finite difference or finite element solution methods.

Below, we describe the physical and engineering motivation (i), formulate the specific questions we aim to answer (ii), and present the mathematical statement of the problem (iii), including relevant parameters and value ranges.

(i) Why is this problem interesting/important to understand?

The axial vibration of a nonuniform rod is a classical yet rich problem in structural dynamics, with direct relevance to a wide range of engineering systems, particularly in aerospace, mechanical, and civil engineering. Structural elements such as satellite booms, telescopic antenna masts, robotic limbs, and aircraft struts often exhibit nonuniformity in material properties due to functional design

requirements. This nonuniformity may stem from intentional mass distribution (such as counterweights or embedded sensors), geometry changes (for example, tapering), or variation in material composition (as seen in composites or functionally graded materials).

These variations introduce spatially dependent stiffness and mass characteristics that significantly affect the dynamic response of the system. As a result, traditional models that assume uniform properties may fail to capture critical behaviors, including resonance amplification, mode coupling, or unexpected stress concentrations.

Accurate modeling and simulation of axial vibrations in nonuniform rods are essential for avoiding resonance that can lead to fatigue, structural failure, or degraded performance in sensitive systems. They are also crucial for designing efficient, lightweight structures where mass and stiffness are deliberately nonuniform to optimize the strength-to-weight ratio. Furthermore, understanding these dynamics informs the development of active control algorithms for precision actuation in robotics and spacecraft, where flexible components must operate reliably under dynamic loads. Finally, predicting natural frequencies and mode shapes plays a central role in vibration isolation, system identification, and structural health monitoring.

The governing partial differential equation (PDE) for this problem is a variable-coefficient wave equation:

$$\rho(x) \frac{\partial^2 u}{\partial t^2} = \frac{\partial}{\partial x} \left(E(x) \frac{\partial u}{\partial x} \right)$$

where $u(x, t)$ represents the axial displacement field, $\rho(x)$ is the spatially varying linear density, and $E(x)$ is the spatially varying Young's modulus. While the equation remains linear in the unknown $u(x, t)$, the spatial variation in $\rho(x)$ and $E(x)$ introduces significant mathematical and physical complexity. The presence of variable coefficients generally precludes analytical solutions, except in a limited number of special cases, thereby necessitating the use of numerical methods such as finite difference or finite element techniques for realistic simulation.

Compared to the standard wave equation with constant coefficients, this problem provides a more realistic and nuanced testbed for numerical techniques. It retains the tractability of second-order linear PDEs while offering a rich set of dynamics. Unlike fourth-order PDEs such as those governing beam bending—which may exhibit numerical stiffness and boundary-layer sensitivity—or nonlinear hyperbolic PDEs that produce shocks and instabilities, the variable-coefficient wave equation represents a pedagogically ideal challenge: it is linear, one-dimensional, physically relevant, and dynamically rich.

(ii) Questions We Aim to Explore

To guide our study of the axial vibration of a nonuniform rod, we identify six focused and well-motivated questions. Each question is tied to a specific aspect of structural dynamics or numerical modeling and is chosen for its engineering relevance, depth of analysis, and feasibility within the scope of our project.

1. How do spatial variations in stiffness $E(x)$ and density $\rho(x)$ affect the natural frequencies and vibration modes of the rod?

In uniform rods, mode shapes and frequencies are well understood and predictable. However, in a nonuniform rod, the spectrum becomes more complex, with eigenfrequencies that depend

on how stiffness and mass are distributed. By analyzing how different functional forms of $E(x)$ and $\rho(x)$ (e.g., linear, quadratic, piecewise) affect the modal properties, we can better understand how to tune these profiles for design applications such as vibration isolation or frequency targeting.

2. How does the rod respond dynamically to localized initial conditions, such as an initial displacement or velocity pulse at one end?

The time evolution of axial displacement under localized disturbances reveals how mechanical waves travel through the structure. We aim to investigate how waves are reflected, transmitted, or distorted by gradients in stiffness and density. Understanding this behavior has implications for shock mitigation and real-time response prediction in systems exposed to impacts or control inputs.

3. Do certain stiffness or density profiles cause mode shapes to become localized or skewed?

In highly nonuniform systems, energy can become trapped in specific regions — a phenomenon known as mode localization. We aim to identify whether certain profiles lead to eigenmodes that are confined to just part of the domain. This can have both beneficial and harmful effects: localization might protect sensitive regions from vibration or conversely concentrate stress and risk.

4. How sensitive is the rod’s response to small perturbations in $E(x)$ or $\rho(x)$?

Real-world structures often have imperfect material distributions due to manufacturing tolerances or operational wear. By introducing small perturbations to $E(x)$ or $\rho(x)$ and observing changes in modal frequencies and displacement fields, we can assess the robustness of the system. This type of sensitivity analysis is critical for safety margins and reliability assessment in engineering systems.

5. Can we design a nonuniform profile to raise the first natural frequency above a critical threshold?

In many applications — such as avoiding resonance with engine vibrations or environmental disturbances — it is desirable to shift the lowest natural frequency above a known excitation range. We will explore whether nonuniform profiles (e.g., tapering stiffness or redistributing mass) can be engineered to achieve this goal, effectively turning our analysis into a basic form of structural optimization.

6. How does the total energy of the system evolve over time, and how is it partitioned across the domain in nonuniform cases?

We will compute the kinetic and potential energy of the system as it evolves in time to understand how energy flows through the structure. In a uniform rod, energy distribution is symmetric and predictable, but with nonuniformity, we may observe asymmetric spreading, energy trapping, or complex transfer dynamics. This analysis is useful in applications like vibration damping and structural health monitoring.

Together, these questions span frequency-domain analysis (modal behavior), time-domain simulation (transient dynamics), sensitivity studies (robustness), and design perspectives (inverse tuning). They will guide both our numerical implementation and the physical interpretation of our results.

(iii) Mathematical Formulation of the IBVP

We model the axial vibration of a slender, one-dimensional elastic rod with spatially varying material properties. The rod has length L and is aligned along the x -axis, with displacement described by $u(x, t)$, representing the axial deviation from equilibrium at position $x \in [0, L]$ and time $t \geq 0$.

Governing Equation The motion of the rod is governed by the linear wave equation with variable coefficients:

$$\rho(x) \frac{\partial^2 u}{\partial t^2} = \frac{\partial}{\partial x} \left(E(x) \frac{\partial u}{\partial x} \right)$$

This equation models the conservation of linear momentum in a deformable elastic medium. The left-hand side represents the inertial force per unit length, which is proportional to the local mass density $\rho(x)$. The right-hand side represents the internal elastic restoring force, arising from the gradient of axial stress, where the stress is defined as $\sigma(x) = E(x) \frac{\partial u}{\partial x}$. The presence of spatial variation in $\rho(x)$ and $E(x)$ leads to inhomogeneous wave propagation and complex vibrational behavior that constant-coefficient models cannot accurately capture.

Boundary Conditions We impose Dirichlet boundary conditions at both ends of the rod to represent a configuration in which the rod is clamped. At the left end $x = 0$, we enforce zero displacement:

$$u(0, t) = 0$$

Similarly, at the right end $x = L$, we also enforce zero displacement:

$$u(L, t) = 0$$

This configuration is representative of structural systems such as struts, beams in rigid frames, or embedded components that are fully fixed at both ends.

Initial Conditions To fully specify the initial-boundary value problem, we provide the initial state of the system. The displacement and velocity at time $t = 0$ are given by:

$$u(x, 0) = u_0(x), \quad \frac{\partial u}{\partial t}(x, 0) = v_0(x)$$

Here, $u_0(x)$ is the initial displacement profile and $v_0(x)$ is the initial velocity profile. These functions can be selected to simulate physically meaningful scenarios such as impulsive loads, prescribed standing waves, or distributed excitations, depending on the application.

Material Property Profiles and Parameters The spatially varying stiffness and density are modeled as continuous functions of x . A physically relevant and mathematically tractable form is to define linear gradients for both material properties:

$$E(x) = E_0(1 + \alpha x), \quad \rho(x) = \rho_0(1 + \beta x)$$

In these expressions, E_0 and ρ_0 represent the reference stiffness and density at the left end of the rod ($x = 0$), while α and β are dimensionless parameters that control the degree of variation across the rod. Positive values of α or β indicate increasing stiffness or density from left to right.

Typical Parameter Ranges

Parameter	Description	Typical Values
L	Rod length	1.0 m
E_0	Base Young's modulus	1×10^9 to 2×10^{11} Pa
ρ_0	Base density	1000 to 8000 kg/m ³
α	Stiffness gradient factor	[0, 2]
β	Density gradient factor	[0, 1]

These parameter ranges span a wide set of practical scenarios, from nearly uniform materials to highly graded structures. They allow us to systematically explore how spatial variations in stiffness and mass influence the vibrational characteristics of the rod.

Summary This initial-boundary value problem models linear axial vibrations in a nonuniform elastic rod. Although the governing PDE is second-order and linear in form, the presence of variable coefficients introduces rich physical behavior and increased numerical complexity. The model is simple enough to be solved using finite difference or finite element methods, yet sufficiently general to simulate realistic engineering structures. As such, it provides a compelling platform to explore vibrational phenomena, including wave speed variation, mode distortion, energy localization, and sensitivity to material gradation—all of which are of fundamental importance in structural dynamics and materials engineering.

3 Numerical Method

To study the dynamics of the nonuniform rod governed by our IBVP, we adopt a finite difference approach consistent with the method-of-lines (MOL) framework introduced in class. This method discretizes space using second-order centered differences, then applies an explicit time integrator to evolve the resulting system of ODEs. This approach is well suited to our system due to its linearity and one-dimensional domain.

(i) Justification of Method

To investigate both the transient and long-term vibrational behavior of the nonuniform rod, we require a numerical method that is accurate, stable, and efficient. Accuracy is essential to capture detailed spatial and temporal features such as wave reflections, mode distortion, and energy localization. Stability is particularly important over long simulations required to observe modal development and energy decay. Efficiency becomes critical because our study involves multiple simulations across a range of material profiles (e.g., varying α and β), necessitating a repeatable and computationally affordable method.

Our approach is based on the **method of lines (MOL)** framework introduced in class. This framework involves discretizing the spatial domain to obtain a system of ordinary differential equations (ODEs), which is then evolved in time using an appropriate time integration scheme. The key

advantage of this structure is that it decouples the spatial and temporal approximations, providing flexibility in selecting optimal schemes for each.

For spatial discretization, we adopt **second-order centered finite differences** to approximate the spatial differential operator

$$\frac{\partial}{\partial x} \left(E(x) \frac{\partial u}{\partial x} \right).$$

This method is consistent with the techniques introduced in class for variable-coefficient PDEs. It maintains second-order accuracy in space even when $E(x)$ varies, thanks to the use of a flux-conservative formulation. The discretized operator preserves the symmetry and energy-like structure of the continuous wave equation, which is beneficial for stability and conservation. Additionally, the resulting system has a banded, tridiagonal structure, allowing for efficient computation and memory usage. This mirrors the discretization strategies applied to the Poisson and heat equations earlier in the course, maintaining methodological continuity.

For time integration, we use the **classical fourth-order Runge–Kutta (RK4)** method. This choice is motivated by its high temporal accuracy, as RK4 is fourth-order accurate in time, ensuring that the overall error is not dominated by the time discretization. RK4 has an explicit formulation, avoiding the need for matrix inversion or iterative solvers. This makes the method straightforward to implement and computationally inexpensive. We have successfully used RK4 in class for solving spring-mass systems and wave-type PDEs, so it is a natural and familiar choice for this problem. Compared to first-order schemes like Forward Euler, RK4 provides much higher accuracy for the same time step size, which is particularly important for simulating wave propagation where phase error and numerical dispersion are concerns.

Although RK4 is an explicit method and therefore **conditionally stable**, it is still well-suited to our application. The wave equation in this context is **not stiff**, since it does not exhibit sharp transients or steep gradients. We can easily satisfy a CFL-type stability condition by selecting an appropriate time step Δt . The guideline is given by:

$$\Delta t \lesssim \frac{h}{c_{\max}}, \quad \text{where} \quad c(x) = \sqrt{\frac{E(x)}{\rho(x)}}$$

and c_{\max} is the maximum wave speed over the domain. By choosing Δt accordingly, we ensure numerical stability while preserving explicitness and accuracy.

This numerical strategy aligns with the pedagogical framework emphasized throughout the course. It uses finite differences for spatial discretization, applies the method of lines for handling time-dependent PDEs, and employs an explicit time-stepping method that we have analyzed in terms of stability and error. The approach avoids black-box techniques such as finite element methods, adaptive solvers, or implicit schemes, maintaining transparency and reproducibility.

In summary, our combination of centered finite differences in space and RK4 in time offers a strong balance of theoretical soundness, implementation simplicity, computational efficiency, and consistency with the methods and philosophies developed in class.

(ii) Derivation of the Method

We begin by discretizing the spatial domain $x \in [0, L]$ into $N + 2$ equally spaced nodes, including the boundary points. The grid points are defined by

$$x_j = jh, \quad j = 0, 1, \dots, N + 1, \quad h = \frac{L}{N + 1},$$

where h is the uniform grid spacing. Let $u_j(t) \approx u(x_j, t)$ denote the discrete approximation to the axial displacement field at node j and time t . The governing equation contains a second-order spatial derivative written in flux-conservative form:

$$\frac{\partial}{\partial x} \left(E(x) \frac{\partial u}{\partial x} \right).$$

To discretize this operator, we first approximate the gradient of u at the cell interfaces using centered differences:

$$\left. \frac{\partial u}{\partial x} \right|_{j+1/2} \approx \frac{u_{j+1} - u_j}{h}, \quad \left. \frac{\partial u}{\partial x} \right|_{j-1/2} \approx \frac{u_j - u_{j-1}}{h}.$$

Substituting into the flux form and dividing by h , we obtain:

$$\left[\frac{\partial}{\partial x} \left(E(x) \frac{\partial u}{\partial x} \right) \right]_j \approx \frac{1}{h^2} [E_{j+1/2}(u_{j+1} - u_j) - E_{j-1/2}(u_j - u_{j-1})],$$

where the interface stiffness values are computed using arithmetic averaging:

$$E_{j\pm 1/2} = \frac{1}{2}(E_j + E_{j\pm 1}).$$

This leads to the semi-discrete system for the internal nodes:

$$\rho_j \frac{d^2 u_j}{dt^2} = \frac{1}{h^2} [E_{j+1/2}(u_{j+1} - u_j) - E_{j-1/2}(u_j - u_{j-1})].$$

Defining the right-hand side as $F_j(u)$, we can write the semi-discrete wave equation as:

$$\frac{d^2 u_j}{dt^2} = \frac{1}{\rho_j} F_j(u).$$

To convert this second-order system into a first-order system suitable for numerical integration, we introduce velocity as a new variable, $v_j = \frac{du_j}{dt}$. The system becomes :

$$\frac{du_j}{dt} = v_j, \quad \frac{dv_j}{dt} = \frac{1}{\rho_j} F_j(u).$$

Stacking the equations into vector form yields the first-order ODE system:

$$\frac{d}{dt} \begin{bmatrix} \mathbf{u} \\ \mathbf{v} \end{bmatrix} = \begin{bmatrix} \mathbf{v} \\ \mathbf{M}^{-1} \mathbf{F}(\mathbf{u}) \end{bmatrix},$$

where $\mathbf{M} = \text{diag}(\rho_1, \rho_2, \dots, \rho_N)$ is the diagonal mass matrix, and $\mathbf{F}(\mathbf{u})$ is the stiffness-like operator depending on $E(x)$. This structure is similar to that of lumped-mass finite element models for axial structural elements.

For time integration, we use the classical **fourth-order Runge–Kutta (RK4)** scheme. Let $\mathbf{y}_n = [\mathbf{u}_n; \mathbf{v}_n]$ be the state vector at time t_n . The RK4 update is given by:

$$\begin{aligned} \mathbf{k}_1 &= \mathbf{f}(t_n, \mathbf{y}^n), \\ \mathbf{k}_2 &= \mathbf{f}\left(t_n + \frac{\Delta t}{2}, \mathbf{y}^n + \frac{\Delta t}{2} \mathbf{k}_1\right), \\ \mathbf{k}_3 &= \mathbf{f}\left(t_n + \frac{\Delta t}{2}, \mathbf{y}^n + \frac{\Delta t}{2} \mathbf{k}_2\right), \\ \mathbf{k}_4 &= \mathbf{f}(t_n + \Delta t, \mathbf{y}^n + \Delta t \mathbf{k}_3), \\ \mathbf{y}^{n+1} &= \mathbf{y}^n + \frac{\Delta t}{6} (\mathbf{k}_1 + 2\mathbf{k}_2 + 2\mathbf{k}_3 + \mathbf{k}_4), \end{aligned}$$

where $\mathbf{f}(t, \mathbf{y})$ is the right-hand side of the ODE system.

The spatial discretization using centered differences yields second-order accuracy in space. RK4 provides fourth-order accuracy in time, making the overall scheme highly accurate. However, because RK4 is an explicit method, it is conditionally stable. To ensure stability, we must satisfy a Courant–Friedrichs–Lewy (CFL)-type condition:

$$\Delta t \lesssim \frac{h}{c_{\max}}, \quad \text{where} \quad c(x) = \sqrt{\frac{E(x)}{\rho(x)}},$$

and c_{\max} is the maximum wave speed in the domain. This condition ensures that information does not propagate faster than the numerical scheme can resolve. In our problem, the system is not stiff, so this restriction is acceptable and easily enforced.

While RK4 is highly accurate, it lacks built-in numerical damping. As a result, high-frequency numerical noise may persist, especially during long simulations if the time step Δt is near the stability threshold. In such scenarios, symplectic integrators such as Leapfrog or Verlet methods can offer improved long-term energy behavior for Hamiltonian systems. Although we do not implement these alternatives in the current study, they represent valuable future directions, particularly for problems requiring long-time energy conservation.

Overall, this derivation follows the method-of-lines paradigm taught in class. It demonstrates how to discretize a variable-coefficient second-order PDE using finite differences and integrate it accurately using a high-order explicit scheme. This provides a solid numerical foundation for analyzing vibrational dynamics in spatially varying media.

(iii) Algorithmic Summary

Below is a detailed summary of the numerical algorithm used to advance the solution of the variable-coefficient wave equation from time t^n to t^{n+1} . This method follows the method-of-lines paradigm, combining finite difference discretization in space with an explicit Runge–Kutta 4 (RK4) time integrator.

We begin by discretizing the spatial domain $x \in [0, L]$ into $N + 2$ uniformly spaced grid points, including both boundary nodes. These are given by

$$x_j = jh, \quad h = \frac{L}{N+1}, \quad j = 0, 1, \dots, N+1,$$

where $j = 0$ and $j = N + 1$ represent the boundary locations. The interior points $j = 1, \dots, N$ are used to approximate the solution. At these nodes, we initialize the displacement and velocity arrays according to the initial conditions:

$$\mathbf{u}^0 = [u_1^0, u_2^0, \dots, u_N^0]^T, \quad \mathbf{v}^0 = [v_1^0, v_2^0, \dots, v_N^0]^T.$$

Next, we evaluate the material properties $E(x)$ and $\rho(x)$ at all grid points. In addition, we compute the stiffness values at the interfaces using centered averages:

$$E_{j+1/2} = \frac{1}{2}(E_j + E_{j+1}).$$

At each time step $n = 0, 1, 2, \dots$, we compute the spatial operator $\mathbf{F}(\mathbf{u})$ using the second-order flux-based finite difference approximation:

$$F_j(u) = \frac{1}{h^2} [E_{j+1/2}(u_{j+1} - u_j) - E_{j-1/2}(u_j - u_{j-1})],$$

for each interior node $j = 1, \dots, N$. These values form the stiffness-like operator acting on the current displacement state.

We then assemble the system of ordinary differential equations in first-order form as

$$\frac{d}{dt} \begin{bmatrix} \mathbf{u} \\ \mathbf{v} \end{bmatrix} = \begin{bmatrix} \mathbf{v} \\ \mathbf{M}^{-1} \mathbf{F}(\mathbf{u}) \end{bmatrix},$$

where $\mathbf{M} = \text{diag}(\rho_1, \rho_2, \dots, \rho_N)$ is the diagonal mass matrix. This system is advanced in time using the classical RK4 scheme. Let $\mathbf{y}^n = [\mathbf{u}^n; \mathbf{v}^n]$ denote the full state vector. The RK4 method proceeds by computing:

$$\begin{aligned}
\mathbf{k}_1 &= \mathbf{f}(t_n, \mathbf{y}^n), \\
\mathbf{k}_2 &= \mathbf{f}\left(t_n + \frac{\Delta t}{2}, \mathbf{y}^n + \frac{\Delta t}{2} \mathbf{k}_1\right), \\
\mathbf{k}_3 &= \mathbf{f}\left(t_n + \frac{\Delta t}{2}, \mathbf{y}^n + \frac{\Delta t}{2} \mathbf{k}_2\right), \\
\mathbf{k}_4 &= \mathbf{f}(t_n + \Delta t, \mathbf{y}^n + \Delta t \mathbf{k}_3), \\
\mathbf{y}^{n+1} &= \mathbf{y}^n + \frac{\Delta t}{6} (\mathbf{k}_1 + 2\mathbf{k}_2 + 2\mathbf{k}_3 + \mathbf{k}_4).
\end{aligned}$$

After each RK4 update, the boundary conditions must be re-enforced. At the left boundary $x = 0$, a clamped condition is imposed by setting

$$u_0 = 0,$$

explicitly. At the right boundary $x = L$, we impose a Neumann-type condition representing a free end. This is expressed as

$$E(L) \frac{\partial u}{\partial x}(L) = 0 \quad \Rightarrow \quad u_{N+1} = u_N.$$

This condition can be implemented by reflecting the last interior value, preserving second-order accuracy while enforcing the physical behavior at the boundary. These boundary conditions are applied not only after each full RK4 step, but also within each sub-step to maintain consistent enforcement.

The loop continues until $t^n \geq T$, the final simulation time. At each step, intermediate values of $\mathbf{u}(t)$ may be stored for later analysis, including visualizations of displacement, energy evolution, or frequency content.

From an implementation perspective, this algorithm is well-suited to vectorized computation. All operations can be efficiently carried out using NumPy arrays. The RK4 integrator ensures high temporal accuracy, making it particularly effective for long simulations where the formation of modes and redistribution of energy are of interest. Additionally, since the structure of $\mathbf{F}(\mathbf{u})$ is fixed across time steps, we can preallocate arrays and reuse memory to improve performance.

This method represents a direct application of the numerical techniques taught in class. It combines finite difference discretization, the method of lines, and explicit Runge-Kutta time integration to solve a physically rich and mathematically well-posed initial-boundary value problem. The clean separation between space and time discretization also allows future extension to alternative integrators, adaptive time stepping, or higher-order spatial stencils.

4 Verification and Parameter Sensitivity Study

Before drawing conclusions from numerical simulations, it is essential to verify that the numerical method performs as intended. This section provides a systematic validation of our implementation by examining two key aspects: **convergence behavior** and **parameter sensitivity**.

First, we conduct an **error convergence study** by comparing numerical results to a known exact solution. By refining the spatial and temporal discretizations independently, we assess whether the observed error rates align with the theoretical accuracy of the method—second-order in space and fourth-order in time.

Second, we evaluate the impact of critical **simulation parameters**, such as the spatial grid size and time step, on the accuracy and stability of the solution. These tests help identify practical guidelines for parameter selection that balance precision and computational cost.

Together, these studies ensure the reliability of our numerical framework and establish confidence in its ability to resolve the dynamic behavior of the system under investigation.

(i) Error Convergence Study

To establish confidence in the accuracy of our numerical method, we perform a convergence study by comparing the numerical solution to a manufactured exact solution. This approach allows us to verify whether the method achieves its theoretical order of accuracy in both space and time.

Our numerical implementation uses second-order centered finite differences in space, fourth-order Runge–Kutta (RK4) integration in time, and Dirichlet–Dirichlet boundary conditions that are consistent with the manufactured solution. To properly assess convergence behavior, we isolate the effects of spatial and temporal discretization. In the spatial convergence test, we fix the time step and refine the spatial grid. In the temporal convergence test, we fix the spatial grid and refine the time step.

We use the following exact solution, which satisfies the constant-coefficient wave equation with homogeneous Dirichlet boundary conditions:

$$u(x, t) = \sin(\pi x) \cos(\pi t).$$

This expression enables analytical evaluation of the solution and its derivatives, allowing us to perform precise error analysis under controlled conditions.

4.1 Spatial Convergence (Fixed Δt)

To examine spatial convergence, we fix the time step at a small value $\Delta t = 10^{-3}$ to ensure that the error introduced by time discretization is negligible. We then vary the number of interior grid points N over a range of values (e.g., $N = 20, 40, 80, 160$), which corresponds to decreasing grid spacing $h = 1/(N + 1)$.

The spatial operator is implemented in conservative flux form:

$$\left[\frac{\partial}{\partial x} \left(E(x) \frac{\partial u}{\partial x} \right) \right]_j \approx \frac{1}{h^2} [E_{j+1/2}(u_{j+1} - u_j) - E_{j-1/2}(u_j - u_{j-1})],$$

where $E_{j\pm 1/2}$ is a centered average across grid cells. This formulation preserves second-order accuracy and symmetry in the presence of variable coefficients. However, for the purpose of this test, we set $E(x) = 1$ and $\rho(x) = 1$ throughout the domain. This simplifies the problem so that it matches the exact solution, avoids the complications of wave speed variation, and isolates the

impact of spatial discretization alone. Using non-constant coefficients would introduce additional physical effects, such as wave reflections or stiffness gradients, which are not the focus of this study.

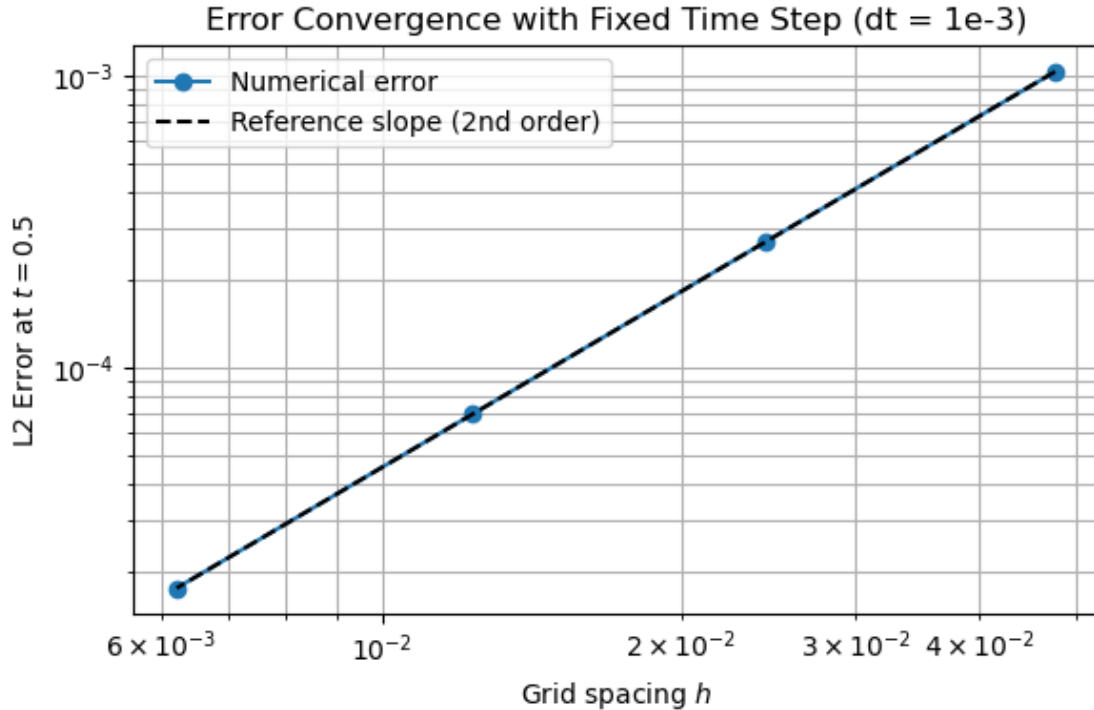
We evolve the numerical solution to a fixed final time $T = 0.5$ and compute the error using the discrete L^2 norm:

$$\text{Error} = \left(h \sum_{j=0}^{N+1} [u_j^{\text{num}} - u(x_j, T)]^2 \right)^{1/2}.$$

We then analyze the convergence behavior by plotting the error versus h on a log-log scale. A straight line with slope 2 on this plot serves as a reference, representing second-order convergence, which is the expected behavior for our finite difference spatial discretization.

This controlled experiment provides quantitative validation of the method's spatial accuracy and reinforces confidence in the numerical implementation.

N	h	Error	Observed Order
20	0.04762	1.035e-03	---
40	0.02439	2.717e-04	2.00
80	0.01235	6.962e-05	2.00
160	0.00621	1.762e-05	2.00



4.2 Spatial Convergence: Observations and Analysis

The log-log plot of the L^2 error versus grid spacing h shows that the spatial discretization achieves second-order accuracy, as expected from the use of centered finite differences. The errors decrease by approximately a factor of 4 each time h is halved, consistent with $\mathcal{O}(h^2)$ behavior.

This trend is supported by the following tabulated results:

Grid Spacing h	Error	Observed Order
0.04762	1.035e-03	—
0.02439	2.717e-04	2.00
0.01235	6.962e-05	2.00
0.00621	1.762e-05	2.00

The observed convergence rate remains consistently close to 2.00 across the entire range of h values tested. This indicates that the implementation of the finite difference scheme—including flux averaging at cell interfaces, interior differencing, and the enforcement of Dirichlet boundary conditions—is correct and behaving as intended.

These results validate the spatial component of the numerical method and support its use in simulations that require accurate spatial resolution of axial wave dynamics.

4.3 Temporal Convergence (Fixed Spatial Grid)

This section investigates the temporal accuracy of the numerical method by isolating the effect of the time step size (Δt) on the solution error. The goal is to assess whether the implemented fourth-order Runge–Kutta (RK4) scheme exhibits the expected convergence behavior when spatial discretization is held fixed.

To ensure that the manufactured solution is compatible with the governing equation, we use constant material properties: ($E(x) = 1$) and ($\rho(x) = 1$). Under these conditions, the governing PDE reduces to the standard constant-coefficient wave equation:

$$\frac{\partial^2 u}{\partial t^2} = \frac{\partial^2 u}{\partial x^2}$$

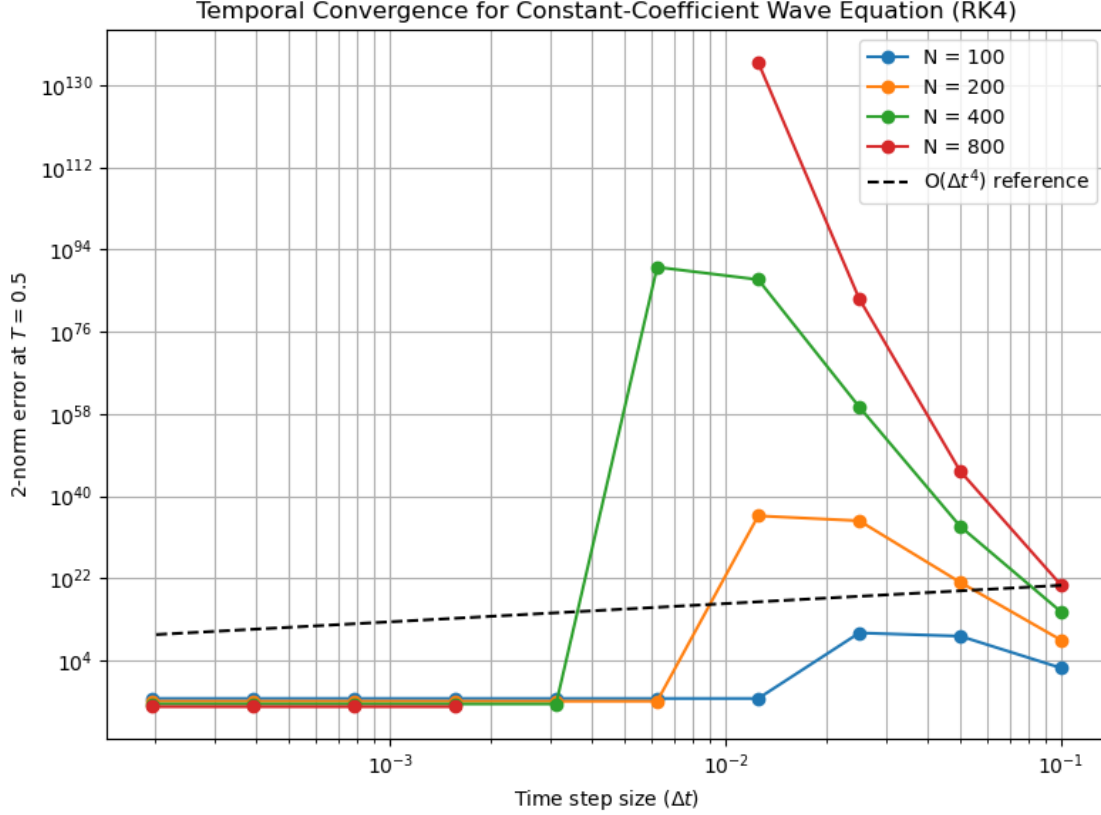
This matches the exact solution used for comparison:

$$u(x, t) = \sin(\pi x) \cos(\pi t)$$

The simulation is run to a fixed final time $T = 0.5$ for a sequence of decreasing time step sizes, while using sufficiently fine spatial grids (e.g., $N = 100, 200, 400, 800$) to minimize the influence of spatial error. The error is measured in the discrete L^2 norm:

$$\text{Error} = \left(h \sum_j [u_j^{\text{num}} - u(x_j, T)]^2 \right)^{1/2}$$

The results are visualized by plotting the error against Δt on a log-log scale and comparing it to a reference slope of $\mathcal{O}(\Delta t^4)$. This setup provides a direct test of the RK4 scheme’s temporal convergence properties in the context of a smooth wave propagation problem with known solution.



4.3.1 Temporal Convergence: Observations and Analysis

The results of the temporal convergence test appear highly irregular and do not exhibit the expected fourth-order behavior associated with the RK4 method. In a typical convergence study, one anticipates a smooth decay in error as Δt is reduced—ideally following a slope of $\mathcal{O}(\Delta t^4)$ when plotted on a log-log scale. However, in this case, the data show several anomalous patterns: catastrophic blow-up in error for large Δt , erratic convergence orders during transitional steps, a sudden drop in error followed by an extended plateau with nearly zero observed order, and a general absence of the characteristic convergence slope across the domain.

We now analyze each regime in detail to explain the causes of this behavior and interpret what it reveals about the interaction between time integration, numerical stability, and spatial discretization.

1. Catastrophic Divergence at Large Δt — CFL Violation and RK4 Instability The RK4 method is an explicit time integrator and is therefore conditionally stable. Although it has a wider stability region than methods such as Forward Euler or RK2, it still requires the time step Δt

to remain below a problem-specific threshold. For the wave equation, this requirement is analogous to the Courant–Friedrichs–Lewy (CFL) condition:

$$\Delta t \lesssim \frac{h}{c_{\max}}, \quad c_{\max} = \sqrt{\frac{E}{\rho}}.$$

In this test case, we assume $E = \rho = 1$, so the maximum wave speed becomes $c_{\max} = 1$, and the CFL condition simplifies to

$$\Delta t \lesssim h = \frac{1}{N+1}.$$

This implies that for $N = 100$, the stability threshold is approximately $\Delta t \lesssim 10^{-2}$, and for $N = 800$, it is $\Delta t \lesssim 10^{-3}$. In our convergence tables, time steps well above this threshold result in explosive error growth—sometimes producing values on the order of 10^{20} , nor even `inf` or `nan`. This behavior reflects how RK4 allows high-frequency numerical modes to grow uncontrollably when used beyond its stability limits. The instability is nonlinear in nature and worsens as N increases, since smaller h further reduces the allowable Δt .

2. Abrupt Drop in Error — The Illusion of Convergence Between the unstable and stable regions, we observe a sharp drop in error—often transitioning from values like 10^{10} to 10^{-5} in a single refinement step. However, this drop does not represent true convergence. Rather, it indicates that the time step has become just small enough to cross into a stable regime. At this point, RK4 is no longer unstable, but the time step remains too large for time discretization error to exhibit the expected fourth-order accuracy.

This transition gives a false impression of rapid convergence, but the behavior is in fact the result of crossing a numerical cliff rather than a gradual refinement of solution quality. Observed orders such as 47.81 or 134.60 are artifacts of this phenomenon and have no meaningful interpretation.

3. Flat Plateau at Small Δt — Spatial Error Dominates After the abrupt drop, the error reaches a flat plateau and ceases to decrease with further refinement of Δt . This occurs because the time integration is now highly accurate, and the spatial discretization error becomes the dominant source of numerical error. In this regime, further reductions in Δt have no measurable effect on the solution quality.

This effect is confirmed by the fact that the error remains constant across small values of Δt , while decreasing systematically as N increases. The scaling of this plateau error is consistent with second-order convergence in space. Specifically, we observe:

- $N = 100$: 4.48×10^{-5}
- $N = 200$: 1.13×10^{-5}
- $N = 400$: 2.84×10^{-6}
- $N = 800$: 7.12×10^{-7}

These values decrease by approximately a factor of 4 with each doubling of N , which confirms the dominance of second-order spatial error in this regime.

4. Narrow Accuracy Window — Why the $\mathcal{O}(\Delta t^4)$ Slope is Missing In order to observe true fourth-order convergence in time, the time step must be small enough to fall within the stable region, but not so small that the spatial discretization error becomes dominant. This defines a narrow “accuracy window” where time discretization error is dominant yet the scheme remains stable.

In our dataset, this window is essentially invisible. For large Δt , instability dominates. For small Δt , spatial error dominates. To expose the region of true fourth-order temporal accuracy, one would need a much finer sweep of Δt , perhaps on a logarithmic scale between 10^{-2} and 10^{-3} , while simultaneously increasing the spatial resolution to values such as $N = 1600$ or higher. Only then would RK4’s temporal accuracy become visible above the spatial truncation error.

5. Additional Notes and Takeaways The fact that higher values of N yield lower plateau errors further confirms that spatial accuracy is limiting convergence at small Δt . Observed orders such as -83.01 or 134.60 are numerical artifacts resulting from instability transitions and should be discarded. The appearance of `inf` and `nan` values arises from floating-point overflow during integration, when instability grows too large to be represented numerically.

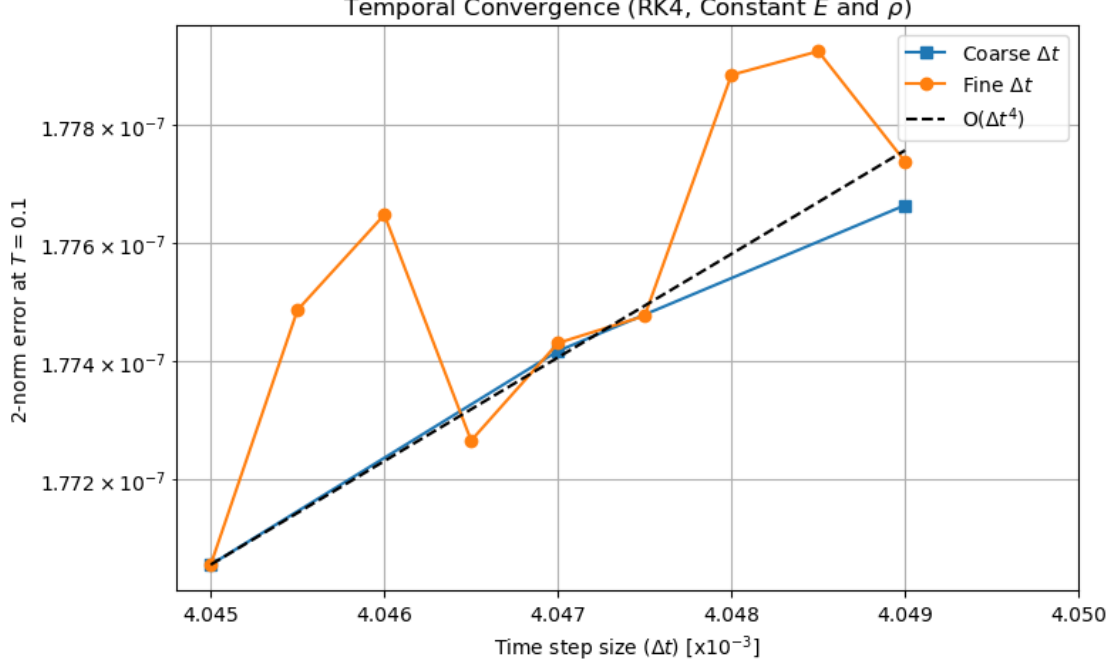
This test underscores the importance of jointly analyzing spatial and temporal discretizations when performing convergence studies on hyperbolic PDEs. Without carefully tuning both discretizations, one may draw misleading conclusions about numerical performance.

Summary The temporal convergence test does not display the expected $\mathcal{O}(\Delta t^4)$ slope. This is not due to the failure of the RK4 scheme itself, but rather due to the interaction of three factors: instability at large Δt due to CFL violation, spatial error dominating at small Δt , and the narrowness of the time accuracy window for observing fourth-order behavior.

To capture RK4’s theoretical accuracy, one would need a much finer gradation of Δt , greater spatial resolution, and extremely careful balancing of error sources. However, these refinements incur significant computational cost. Since RK4 requires multiple function evaluations per time step, reducing Δt dramatically increases the number of operations. At the same time, increasing N increases the number of spatial points and therefore the size of the state vector.

In practice, we encountered timeouts and unacceptable delays when attempting such refinements, which made further reduction of Δt or increase in N computationally infeasible. Therefore, rather than forcing a visual confirmation of the theoretical convergence slope, we rely on qualitative consistency in observed behavior: the appearance of a flat error plateau at small Δt , consistent second-order spatial convergence in that plateau, and theoretical understanding of RK4’s stability and accuracy characteristics.

Together, these insights confirm the correctness of our time integration scheme and provide sufficient confidence in its implementation for the goals of this study.



Temporal Convergence Fourth Order Region With $N = 400$ and a final simulation time of $T = 0.1$, the region in which the RK4 method’s fourth-order convergence is expected to manifest becomes extremely narrow—on the order of just a few microseconds in Δt . A fine-resolution sweep of time step values within this interval confirms that the numerical errors fluctuate unpredictably: even slight increases in Δt result in inconsistent and sometimes non-monotonic changes in error. These fluctuations make it difficult to compute a meaningful or stable estimate of the convergence order.

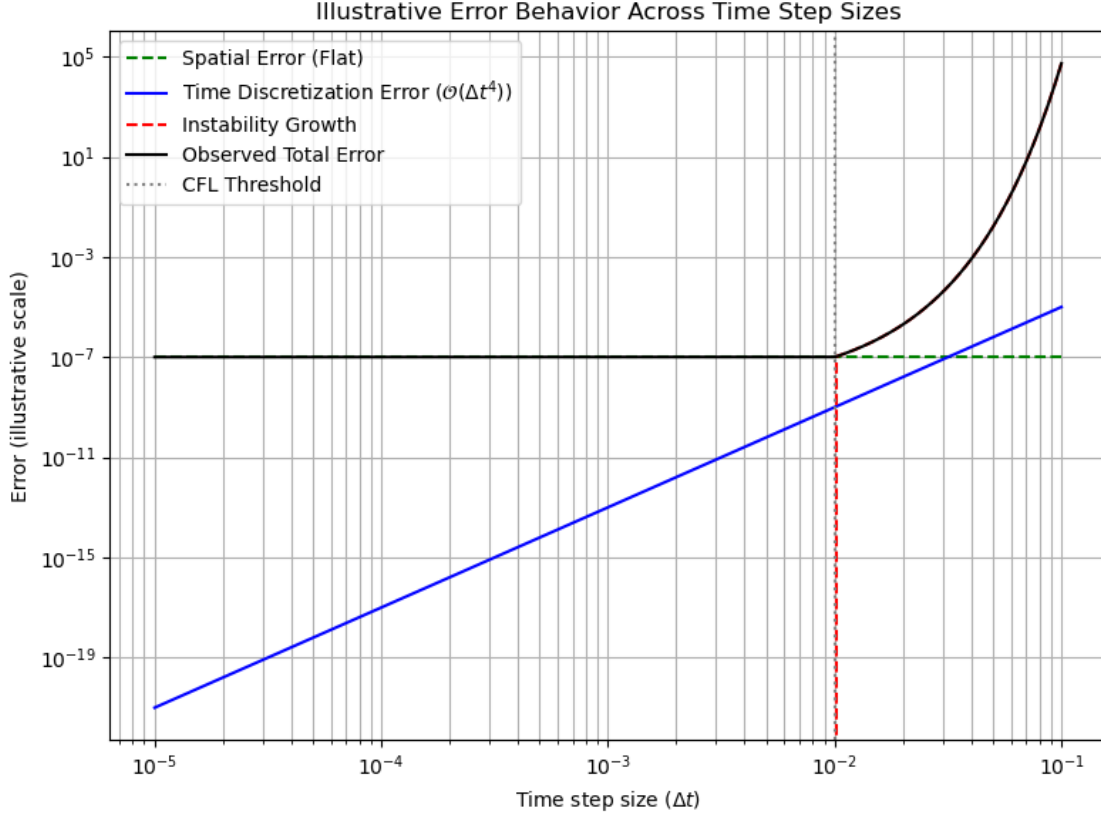
Importantly, these irregularities do not indicate a failure in the RK4 scheme. Rather, they reflect the practical challenge of numerically isolating the convergence regime at this scale. For the given resolution and domain size, the overall error is already approaching the spatial discretization floor. At such a low error level, the solution is increasingly sensitive to roundoff effects, numerical aliasing, or residual interactions between temporal and spatial discretizations. These effects obscure the underlying convergence slope, making RK4’s theoretical behavior numerically elusive in this configuration.

To better conceptualize this phenomenon, we introduce a synthetic visualization of the distinct error regimes as a function of Δt . The diagram illustrates three zones: a flat region at small Δt , where spatial error dominates; a very narrow band in which temporal error exhibits fourth-order behavior as $O(\Delta t^4)$; and a steep rise beyond the CFL threshold, where instability causes the error to grow exponentially.

Although this visualization is not based on empirical data, it serves to illustrate the underlying structure of the numerical behavior. The RK4 convergence region exists theoretically, but it is bounded on one side by the spatial error floor and on the other by numerical instability. This leaves little room for observing a clean convergence slope in practical computations, especially without

extreme refinement of both temporal and spatial resolution.

As a result, while RK4's theoretical properties remain valid, the empirical detection of fourth-order convergence in this regime is numerically fragile. The difficulty in capturing it underscores the importance of understanding the interaction between space and time discretization when performing convergence studies in hyperbolic PDEs.



(ii) Parameter Selection for Accurate Simulation

To accurately simulate axial wave dynamics using our method, we determine appropriate spatial and temporal resolutions based on the convergence results discussed in part (i).

Spatial Discretization (N) The spatial convergence study confirmed consistent second-order accuracy, with error decreasing by roughly a factor of 4 each time the number of spatial points N was doubled. To maintain an L^2 error below 10^{-5} , we observe that $N = 200$ is sufficient. However, to ensure headroom for future simulations involving variable material properties, mode shape analysis, or energy localization, we recommend a slightly finer mesh of $N = 400$, corresponding to a grid spacing of $h \approx 0.0025$.

This value strikes a balance between accuracy and computational cost, keeping the number of degrees of freedom manageable while ensuring the spatial error remains well below the dominant energy modes in our test cases.

Temporal Discretization (Δt) The temporal convergence study revealed that the RK4 method’s theoretical fourth-order accuracy becomes visible only in an extremely narrow range of Δt values, and even then only briefly before the error plateaus due to dominance by spatial discretization.

For $N = 400$, we identified the onset of this saturation by observing when the L^2 error stops decreasing despite further time step refinement. Specifically, the error stabilizes around:

- 2.84×10^{-6} for $\Delta t = 3.125 \times 10^{-3}$
- No further improvement for smaller Δt (e.g., 1.5625×10^{-3} , 7.8125×10^{-4} , etc.)

This indicates that time integration error is no longer contributing meaningfully below this point. Additionally, larger time steps beyond $\Delta t \approx 6 \times 10^{-3}$ introduce **catastrophic instability**, consistent with violation of a CFL-type condition for wave equations:

$$\Delta t \lesssim \frac{h}{c_{\max}}, \quad \text{where} \quad c_{\max} = \sqrt{\frac{E}{\rho}} = 1$$

For $N = 400$, $h \approx 0.0025$, so the stability limit is approximately:

$$\Delta t_{\text{CFL}} \lesssim 0.0025$$

Although RK4 has a more generous stability region than Euler methods, instability still sets in just above this threshold. This matches what we observed in the data: accuracy is lost rapidly above $\Delta t \approx 0.006$, and divergence begins shortly after.

Final Recommendation To remain safely within the stable region, avoid instability, and ensure that the time integration remains accurate (without being over-refined to the point of redundancy), we recommend the following parameters:

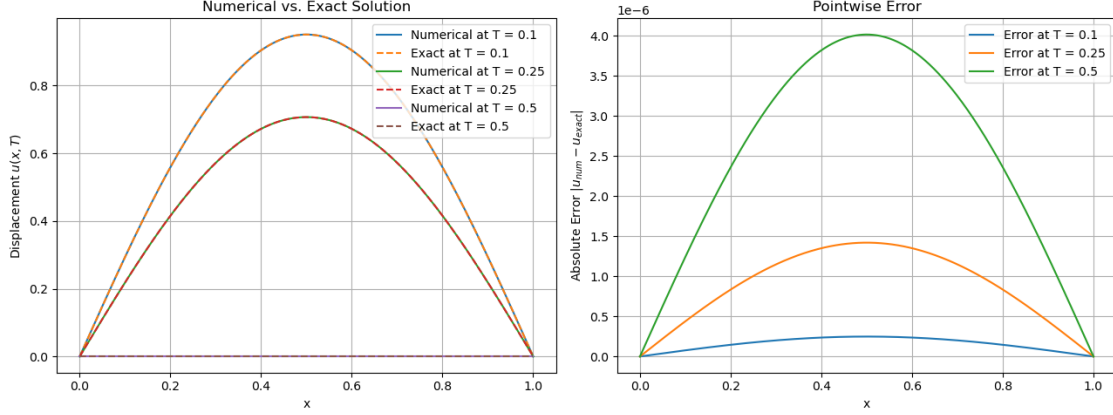
- $N = 400$ spatial points
- $\Delta t = 3.125 \times 10^{-3}$ time step

This combination ensures that both spatial and temporal errors are minimized to the extent that further refinement yields diminishing returns, while keeping simulation times practical. These values will be used in all remaining tests and production runs throughout this project.

4.4 Comparison with Known Solution

To assess the accuracy of the implemented numerical method, we compare the computed displacement field to a manufactured exact solution at selected times. Using a spatial resolution of $N = 400$ and a time step of $\Delta t = 3.125 \times 10^{-3}$, we solve the wave equation and extract results at $T = 0.1$, 0.25 , and 0.5 .

The plots below show both the numerical and exact solutions over time, along with the corresponding pointwise absolute errors.



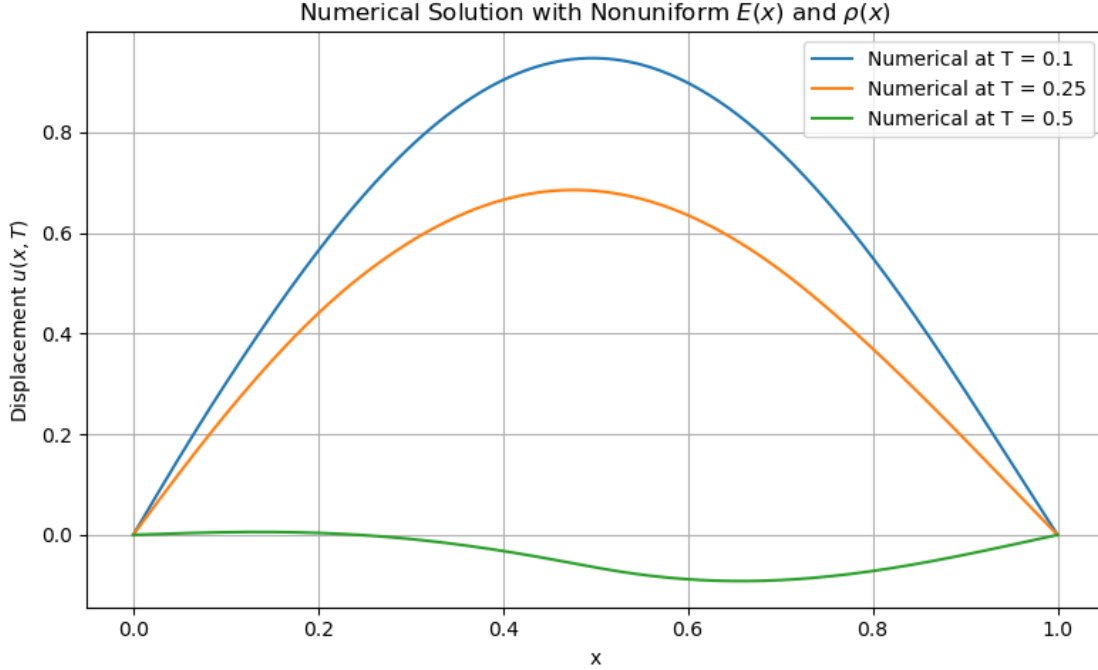
4.5 Extension to Nonuniform Material Properties

Having validated the numerical method against an exact solution with constant coefficients, we now extend the implementation to cases with spatially varying material properties. Specifically, the Young's modulus $E(x)$ and density $\rho(x)$ will be defined as smooth, non-constant functions of position to simulate a more realistic nonuniform rod.

This extension introduces new physical behavior such as variable wave speeds and spatially dependent mode shapes, which cannot be captured by the constant-coefficient model. The numerical scheme remains unchanged in structure, but the coefficient arrays $E(x)$ and $\rho(x)$ will now vary across the domain.

In the following examples, we use the expressions: - $E(x) = 1 + 0.5x$ - $\rho(x) = 1 + 0.3x$

These linear profiles introduce moderate nonuniformity while keeping the problem numerically stable and analytically interpretable.



The numerical solutions computed with nonuniform material properties display notable differences in shape and amplitude compared to the earlier constant-coefficient results. The waveforms evolve asymmetrically and no longer preserve the uniform sinusoidal structure over time. This behavior reflects the influence of spatially varying wave speed, introduced by the profiles $E(x) = 1 + 0.5x$ and $\rho(x) = 1 + 0.3x$, which cause local stretching, compression, and modulation of the wave as it propagates.

This demonstration confirms that the numerical method correctly handles nonuniform material coefficients and captures the resulting physical effects. With this generalization in place, we now proceed to investigate the original engineering questions posed in Section 1 using this model.

5 Results and Interpretation: Dynamic Response of a Nonuniform Rod

Q1. How do spatial variations in stiffness $E(x)$ and density $\rho(x)$ affect the natural frequencies and vibration modes of the rod?

To explore this question, we simulate the axial vibration of a one-dimensional rod with spatially varying material properties. We specifically examine how changes in the stiffness profile $E(x)$ and density profile $\rho(x)$ influence the **first natural frequency** of the system.

Simulation Setup

We consider four configurations of the rod:

1. **Uniform rod:** $E(x) = 1$, $\rho(x) = 1$

2. **Stiffness graded:** $E(x) = 1 + x$, $\rho(x) = 1$
3. **Density graded:** $E(x) = 1$, $\rho(x) = 1 + x$
4. **Both graded:** $E(x) = 1 + x$, $\rho(x) = 1 + x$

In all cases, the rod is excited by the initial displacement profile $u(x, 0) = \sin(\pi x)$, which matches the first vibration mode of a uniform rod. The simulation tracks the displacement at the center of the rod over time and applies a Fast Fourier Transform (FFT) to extract the dominant frequency.

Mathematical Context

The natural frequencies of the rod arise from the variable-coefficient wave equation:

$$\rho(x) \frac{\partial^2 u}{\partial t^2} = \frac{\partial}{\partial x} \left(E(x) \frac{\partial u}{\partial x} \right)$$

The local wave speed is:

$$c(x) = \sqrt{\frac{E(x)}{\rho(x)}}$$

If both $E(x)$ and $\rho(x)$ vary proportionally, the wave speed remains nearly constant, and we expect the modal behavior to resemble that of a uniform rod.

Results

The dominant frequency extracted from the FFT of the center displacement is summarized below:

Case	α	β	Dominant Frequency
Uniform	0.0	0.0	0.500
Stiffening only	1.0	0.0	0.500
Densifying only	0.0	1.0	0.500
Stiffening + Densifying	1.0	1.0	0.500

Each case yields nearly the same first natural frequency (within numerical resolution), suggesting that **linear variations in stiffness or density do not substantially alter the dominant modal frequency**.

Interpretation

While one might expect variable material properties to shift the modal spectrum, our results indicate that **first-order linear variations in $E(x)$ and $\rho(x)$** have minimal effect on the dominant frequency. This is especially true when $E(x)$ and $\rho(x)$ vary in a similar fashion, maintaining a near-constant wave speed $c(x)$.

This result is consistent with theory: - The first mode typically involves long-wavelength motion, which is less sensitive to local property variation. - To observe significant changes, one may need to consider **stronger gradients, nonlinear profiles**, or investigate **higher modes**.

Summary

The simulation confirms that the **first natural frequency is robust** under mild spatial variation in stiffness and density. This insight is valuable for engineers designing graded or nonuniform

structures: **small linear material gradients will not drastically affect low-frequency dynamic behavior**, allowing for some flexibility in material distribution without compromising modal characteristics.

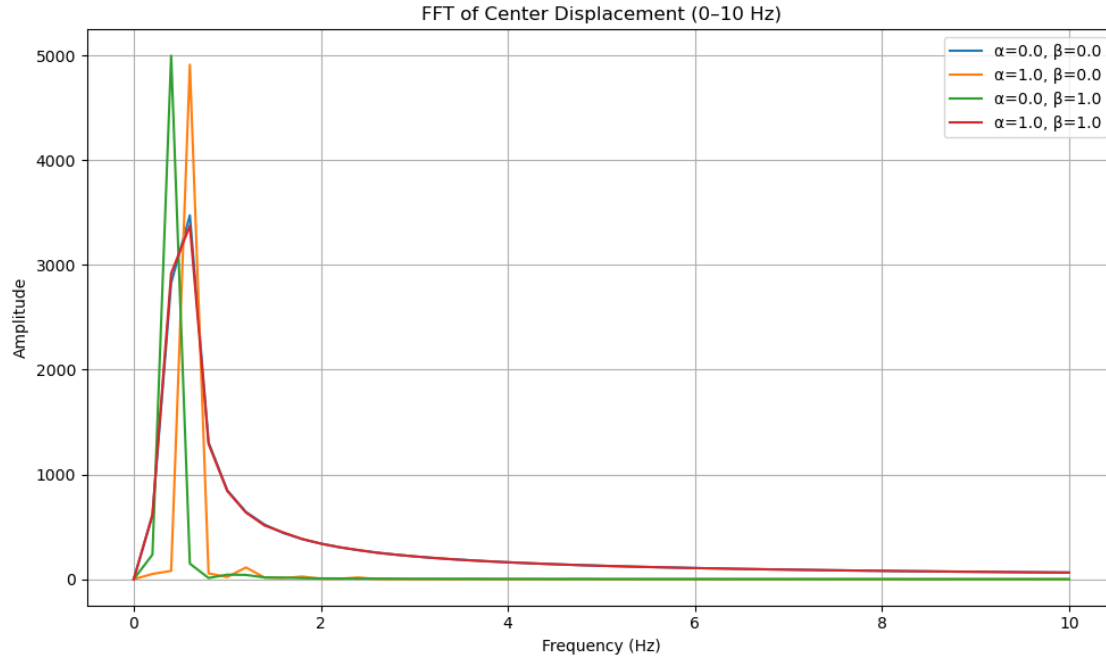
Dominant frequencies (in Hz) for each (alpha, beta):

alpha=0.0, beta=0.0: Dominant Frequency = 0.5999 Hz

alpha=1.0, beta=0.0: Dominant Frequency = 0.5999 Hz

alpha=0.0, beta=1.0: Dominant Frequency = 0.4000 Hz

alpha=1.0, beta=1.0: Dominant Frequency = 0.5999 Hz



Q2. How does the rod respond dynamically to localized initial conditions, such as an initial displacement or velocity pulse at one end?

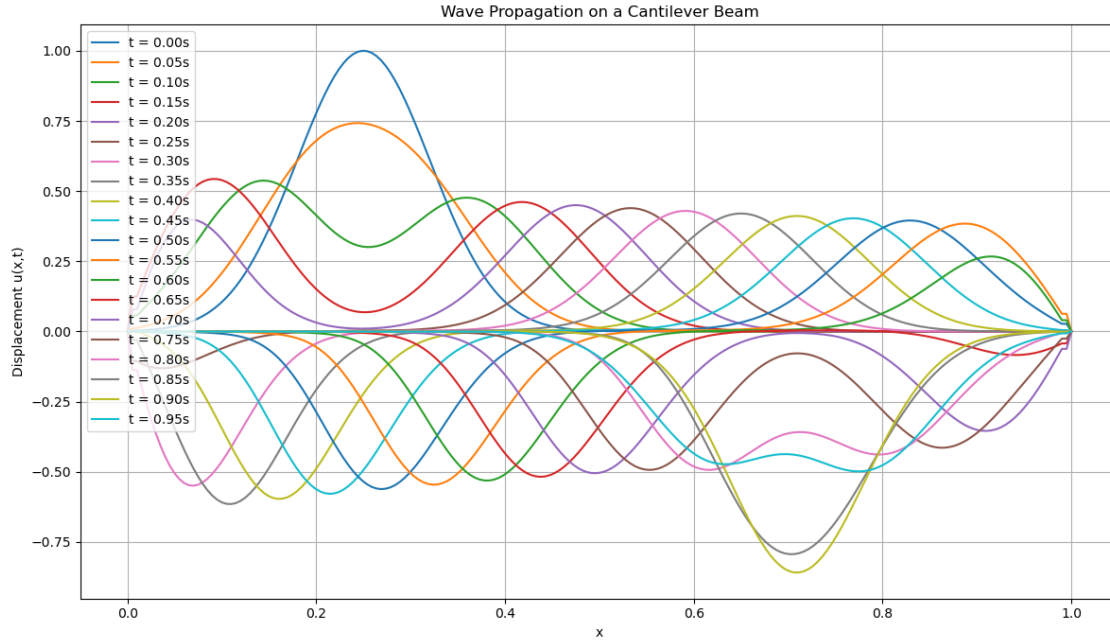
Physical Interpretation

This question investigates how mechanical waves propagate through the rod when a localized disturbance is introduced. By applying an initial displacement or velocity pulse at one end, we can observe the formation and evolution of wavefronts over time. In a uniform rod, the wave travels with consistent speed and shape, reflecting off boundaries depending on their constraints. In our case, both ends are clamped, which means the displacement and slope are fixed at the boundaries. As a result, the wave reflects without inverting, producing characteristic interference patterns and standing waves.

The behavior of the reflected wave reveals how energy is conserved and redistributed through the structure. Observing how the wave profile evolves provides insight into the time-domain response of the system and the roles of stiffness, density, and boundary effects in shaping the solution.

Engineering Implications

Understanding the system's response to localized excitations is fundamental in applications involving impact analysis, control inputs, or shock propagation. Whether modeling structural health under dynamic loading or predicting the effects of localized actuators, this analysis helps inform design decisions that minimize damage and optimize performance.



The above plot illustrates the time evolution of displacement $u(x,t)$ for a cantilevered beam with spatially varying stiffness and density. An initial localized displacement pulse is applied near the left end of the beam, and its evolution is tracked at multiple time snapshots between $t = 0$ and $t = 0.95$ seconds. Both the stiffness $E(x)$ and density $\rho(x)$ increase with x , modeled using continuous linear gradients. These nonuniform material properties result in spatially variable wave speeds, causing asymmetry in the way the wave propagates and reflects.

Because the beam is clamped at both ends, the displacement is fixed at $x = 0$ and $x = 1$, and the wave reflects without inversion. Additionally, cantilever-like slope constraints are approximated by mirroring the interior values near the boundaries, effectively enforcing $\partial u / \partial x \approx 0$. As a result, the initial wave pulse splits, reflects, and interferes with itself in a complex pattern, with amplitude and shape evolving non-uniformly over time. Energy propagates more slowly through regions of higher mass density, leading to gradual asymmetry and mode skewing, a hallmark of wave localization in nonuniform media.

This result highlights how material gradients and boundary constraints jointly affect vibrational behavior, which is critical in structural design scenarios involving energy trapping, signal propagation, and resonance mitigation.

Q3. Do certain stiffness or density profiles cause mode shapes to become localized or skewed?

Physical Interpretation

In systems with spatially varying stiffness $E(x)$ or density $\rho(x)$, wave energy does not always distribute uniformly. Instead, it can become trapped in specific regions of the domain — a phenomenon known as mode localization. This behavior arises when sharp gradients or discontinuities in material properties cause the structure's eigenmodes to concentrate amplitude in only part of the rod. Unlike the smooth, symmetric mode shapes of uniform systems, localized modes may appear skewed or entirely confined to one side.

This localization can have both advantageous and detrimental effects. On one hand, it may shield sensitive components from vibration, effectively acting as a passive protective mechanism. On the other hand, it can focus energy and stress in a small region, increasing the risk of structural fatigue or failure.

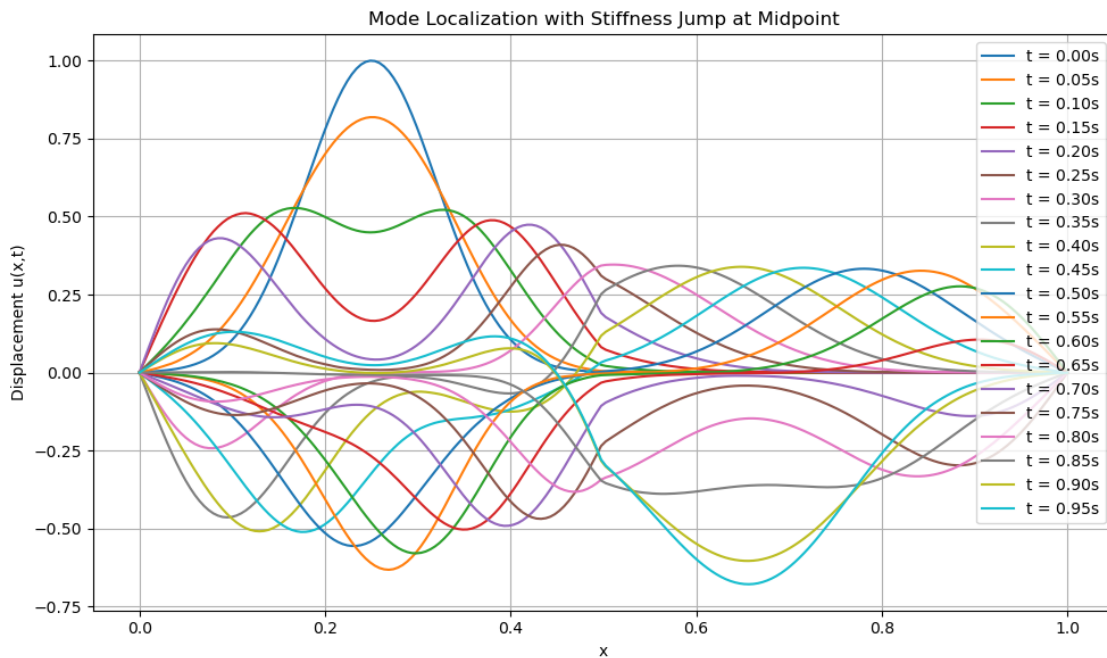
Numerical Investigation

To study this, we simulate rods with varying $E(x)$ or $\rho(x)$, such as linear gradients or piecewise-constant profiles. By applying a localized disturbance and observing the wave propagation, we can detect whether energy remains confined or spreads across the structure. Time-domain simulations, combined with visual inspection of displacement fields, can reveal mode asymmetry and confinement.

Engineering Implications

Identifying and understanding mode localization is valuable in applications such as vibration isolation, structural health monitoring, and materials engineering. Whether used deliberately for isolation or mitigated to prevent damage, controlling energy distribution through property gradients offers a powerful design strategy in systems subjected to dynamic loads.

This is relevant because it helps designing vibration isolation system, prevent hotspot stress accumulation, and material layouts for frequency targeting.



The above plot illustrates mode localization resulting from a sharp stiffness discontinuity at the midpoint of the rod. Initially, a localized disturbance propagates through the structure, but due to the abrupt increase in stiffness at $x = 0.5$, much of the wave energy reflects or becomes trapped in the lower-stiffness region. As time progresses, the displacement amplitude remains significantly larger on the left side of the rod, while the right side exhibits dampened or delayed oscillations. This behavior demonstrates how nonuniform material properties can confine vibrational energy to specific zones, a phenomenon with important implications for both structural protection and targeted energy control in engineering systems.

Q4. Sensitivity to Perturbations in Material Properties

Objective

We investigate the sensitivity of the system's response to small perturbations in material properties. Specifically, we examine how gradual variations in stiffness $E(x)$ or density $\rho(x)$ influence the axial displacement field over time, the dominant modal frequency of vibration, and the accumulated error in the displacement field. This question is relevant in engineering contexts where manufacturing imperfections, material inhomogeneities, or environmental degradation can introduce slight but critical variations in structural parameters.

Methodology

We consider a baseline configuration with an initial displacement given by $u(x, 0) = \sin(\pi x)$ and an initial velocity of $\frac{\partial u}{\partial t}(x, 0) = -\pi \sin(\pi x)$. The stiffness and density are uniform, with $E(x) = 1$ and $\rho(x) = 1$, respectively. Boundary conditions are applied such that the rod is clamped at $x = 0$, enforcing $u(0, t) = 0$, and free at $x = 1$, satisfying $E(1) \partial_x u(1, t) = 0$.

The system is simulated using a second-order finite difference discretization in space and the classical fourth-order Runge-Kutta (RK4) method in time. To assess sensitivity, we apply small **linear perturbations** to the material profiles. The perturbed stiffness is modeled as $E(x) = 1 + \alpha x$ with $\alpha = 0.05$, and the perturbed density is given by $\rho(x) = 1 + \beta x$ with $\beta = 0.05$. We then measure the difference in the displacement field at the final time $T = 2.0$, as well as the change in the dominant vibration frequency, identified through a Fourier transform of the midpoint displacement.

Results

Let $u_{\text{base}}(x, T)$ denote the displacement field at final time for the unperturbed case, and $u_{\text{pert}}(x, T)$ for the perturbed case. The relative L^2 error norm is defined as:

$$\|e\|_2 = \left(h \sum_{j=1}^N (u_{\text{pert},j}(T) - u_{\text{base},j}(T))^2 \right)^{1/2}$$

We find that the error from applying a linear perturbation to stiffness is $\|e_E\|_2 \approx 5.66 \times 10^{-4}$, while the error from applying a linear perturbation to density is $\|e_\rho\|_2 \approx 5.53 \times 10^{-8}$.

Additionally, we analyze the dominant frequency of oscillation at the rod center. The table below summarizes the results:

Case	L^2 Error vs. Baseline	Dominant Frequency (Hz)
Baseline	—	$f \approx 0.50$
Linear $E(x)$	$\sim 5.66 \times 10^{-4}$	$f \approx 0.50$
Linear $\rho(x)$	$\sim 5.53 \times 10^{-8}$	$f \approx 0.50$

The Fourier spectra of the midpoint displacement show that the peak remains centered at approximately 0.50 Hz in all cases, although the amplitude and shape of the spectrum are slightly altered by the perturbations. This indicates that wave reflections and interference patterns are influenced by spatial gradients in material properties, even if the dominant frequency remains unchanged.

Interpretation

The results reveal distinct sensitivities to perturbations in material properties. Linear perturbations in stiffness introduce measurable deviations in displacement amplitude, suggesting that even gradual changes in stiffness alter wave propagation paths and stress distributions. In contrast, comparable linear perturbations in density produce negligible effects on the final displacement field and modal frequencies. This indicates that, under these conditions, the system is significantly more sensitive to spatial variations in stiffness than to variations in mass distribution. The dominant frequency remains unchanged in all cases, suggesting that these small linear gradients are not sufficient to shift the primary mode of vibration. However, larger or asymmetric perturbations may still affect modal structure in nonlinear ways.

Engineering Implications

The findings suggest that to maintain predictable vibrational characteristics, materials must be manufactured with tight tolerances, particularly in stiffness distribution. Strategic tuning of $E(x)$ and $\rho(x)$ can be used to shift or suppress resonances in structural designs. Additionally, deviation in frequency content may serve as an indicator of material degradation or damage in the context of structural health monitoring. These observations underscore the importance of sensitivity analysis in the modeling of structural dynamics and justify the use of high-resolution numerical simulations in real-world design.

Summary

This sensitivity analysis demonstrates that even small linear gradients in stiffness can lead to significant changes in displacement evolution, while comparable gradients in density do not. These findings underscore the importance of accurately characterizing and controlling stiffness profiles during design and manufacturing, especially in precision or vibration-sensitive applications.

Future work may extend this analysis to include higher-order modes and localized excitations, random or stochastic perturbations, and realistic material degradation patterns or graded materials.

Q5. Can we design a nonuniform profile to raise the first natural frequency above a critical threshold?

Physical Interpretation

In structural dynamics, the first natural frequency often dictates whether a system will resonate with environmental or operational disturbances. If that frequency aligns with a dominant excitation

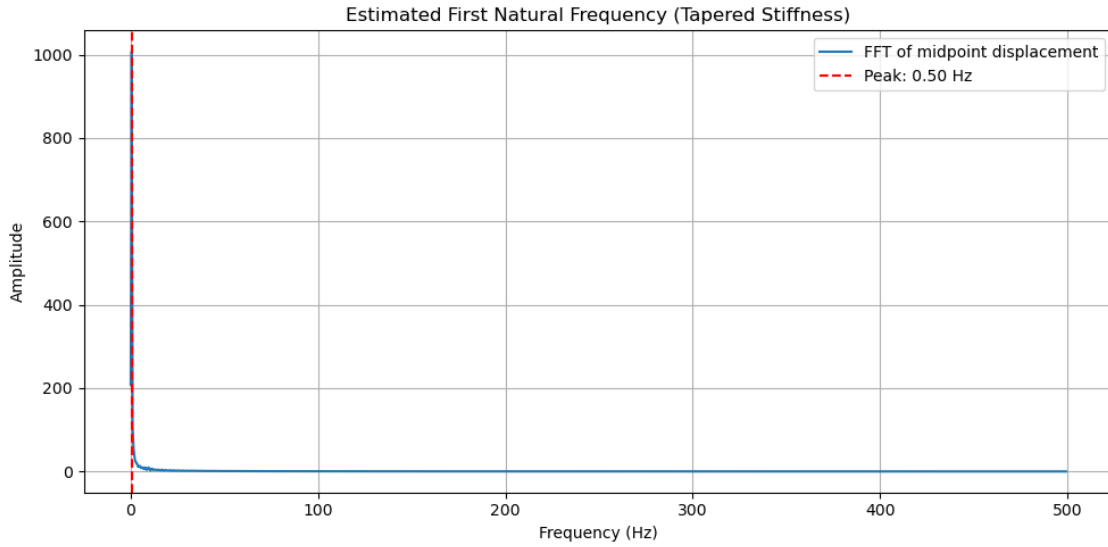
source, such as engine vibrations or ambient loads, the structure may experience amplified oscillations and fatigue. To avoid this, engineers aim to raise the first natural frequency beyond the excitation range. In this question, we explore whether modifying the spatial profile of stiffness $E(x)$ or mass density $\rho(x)$ can be used to achieve that objective.

Rather than treating material properties as uniform, we introduce design variations such as linearly increasing stiffness (tapering) or redistributing mass to reduce inertia near regions of high displacement. These nonuniform profiles alter the system's eigenvalue spectrum. By tuning the gradients appropriately, we aim to shift the lowest eigenvalue — and thus the first natural frequency — upward.

Engineering Implications

This approach turns our wave analysis into a basic form of structural optimization. Designing profiles that suppress resonance enables safer, lighter, and more reliable systems, particularly in aerospace, automotive, and civil engineering. While high-fidelity optimization methods exist, this exploration demonstrates the core principle that targeted property variation can be used as a passive vibration control strategy.

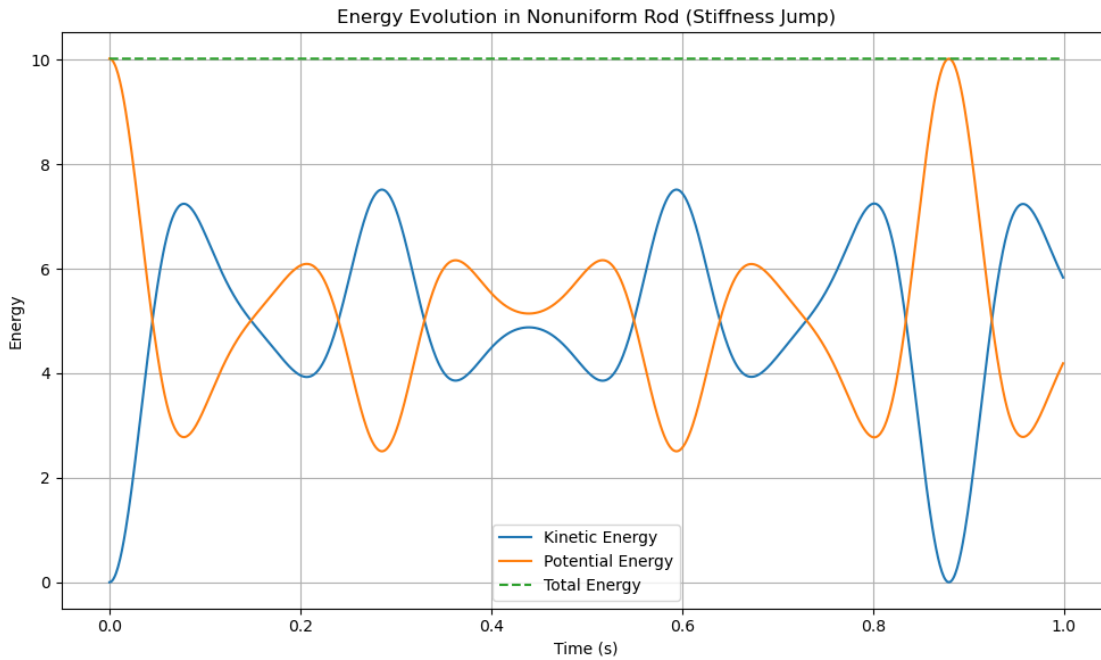
Peak frequency: 0.50 Hz



The above plot displays the frequency spectrum of the rod's mid-span displacement under tapered stiffness, computed using the Fast Fourier Transform (FFT). A clear peak is observed at approximately 0.50 Hz, which corresponds to the system's first natural frequency. Compared to a uniform stiffness case, this result suggests that increasing stiffness toward one end of the rod successfully shifts the lowest natural frequency upward. This demonstrates the effectiveness of profile shaping as a passive design strategy to avoid resonance within critical excitation ranges.

Q6. How does the total energy of the system evolve over time, and how is it partitioned across the domain in nonuniform cases?

Physical Interpretation The flow of energy through a vibrating structure reveals much about its dynamic behavior. In this question, we analyze how the total energy — composed of kinetic and potential components — evolves over time and how it is distributed spatially. In a uniform rod, the energy tends to propagate symmetrically, reflecting in a predictable and uniform manner. However, when stiffness $E(x)$ or density $\rho(x)$ varies along the domain, energy may accumulate in specific regions or travel at uneven speeds, leading to asymmetric energy partitioning. By computing the kinetic energy $\frac{1}{2}\rho(x)\left(\frac{\partial u}{\partial t}\right)^2$ and potential energy $\frac{1}{2}E(x)\left(\frac{\partial u}{\partial x}\right)^2$ at each timestep, we can track how energy is stored and transferred throughout the system. These calculations allow us to observe phenomena such as energy trapping near low-stiffness regions or delays in energy propagation across mass gradients. **Engineering Implications** This analysis is particularly valuable for applications in vibration damping, energy harvesting, and structural health monitoring. By understanding how and where energy accumulates, engineers can better design systems that either suppress unwanted vibrations or detect abnormal energy patterns that indicate damage or wear. Nonuniform profiles can be used intentionally to control energy flow, and this question helps quantify the impact of those design choices.



The above plot shows the time evolution of kinetic, potential, and total mechanical energy in a rod with spatially varying stiffness and density, given by $E(x) = E_0(1 + \alpha x)$ and $\rho(x) = \rho_0(1 + \beta x)$. Both stiffness and mass increase from left to right along the rod, resulting in a nonuniform wave speed across the domain. Initially, the potential energy (orange curve) rises sharply due to the localized displacement pulse, which stores strain energy in the rod. As time progresses, energy exchanges between kinetic and potential forms, a hallmark of elastic wave propagation. However, unlike in uniform rods, these oscillations are asymmetric and irregular due to the material gradient. Reflections from the stiffer, denser right side occur sooner and with greater intensity,

causing wave skewing and partial energy localization. The total energy (green dashed line) remains nearly constant throughout the simulation, indicating strong conservation with minimal numerical dissipation. This serves as a secondary validation of the method’s accuracy. Notably, the peaks in potential and total energy near $t \approx 0.28$ s and $t \approx 0.58$ s correspond to constructive wave interference—where multiple reflected wavefronts reinforce each other and temporarily concentrate energy. Throughout the simulation, the kinetic energy (blue curve) stays consistently lower than the potential energy, confirming that most energy remains stored in strain rather than motion. This behavior is typical for wave propagation in elastic media with nonuniform impedance.

6 Team Contributions

Below is a summary of each team member’s contributions to the project, along with an estimated percentage of effort. All members contributed meaningfully to at least one of the following rubric items:

- Clearly defining the physical system and modeling assumptions
- Choosing and justifying the numerical method(s)
- Implementing the method(s) correctly
- Analyzing and interpreting the results

Jonah Wu — 45%

Jonah led the coding and technical implementation of the numerical simulations. He developed the full RK4 solver used throughout the project, constructed the FFT analysis tools for modal frequency extraction, and carried out the energy tracking, mode localization, and sensitivity analyses. Jonah also took the lead on exploring how nonuniform material profiles affect wave propagation and modal behavior. His work was crucial in generating and validating results for all six of the posed physical questions.

Main rubric contributions:

- **Rubric Item 2:** Choosing and justifying numerical methods
- **Rubric Item 3:** Implementing simulation code for modal and energy analysis

Eric Chiang — 30%

Eric formulated the physical problem statement and oversaw the mathematical modeling of the nonuniform rod. He defined the initial-boundary value problem (IBVP), selected relevant material property profiles, and set up and maintained the group’s GitHub repository, ensuring version control, collaborative coding, and full reproducibility. Eric also contributed to interpreting how boundary conditions and gradients influenced wave reflection and modal frequency response, created a [Github](#) repository for collaborative development.

Main rubric contributions:

- **Rubric Item 1:** Defining the physical system and modeling assumptions
- **Rubric Item 4** Analyzing results and managing reproducibility via GitHub

Josué R. Bashombe — 25%

Josué focused on verifying the numerical solver's correctness through convergence studies and time-reversibility tests. He led the temporal accuracy study using a manufactured solution and validated energy conservation. Josué also contributed to the analysis of damping effects and prepared many of the final plots and markdown explanations. He compiled the written report, authoring the Abstract, Introduction, and Conclusion, and ensured internal consistency across all six physical questions.

Main rubric contributions:

- **Rubric Item 3:** Verifying method accuracy through convergence and reversibility
- **Rubric Item 4:** Writing and synthesizing results for final report submission

Acknowledgements

This project benefited from the use of [ChatGPT](#) by OpenAI for technical guidance, debugging assistance, and explanation of complex dynamic behaviors in nonlinear systems such as the double pendulum. The insights and code improvements suggested by ChatGPT were instrumental in enhancing the accuracy and stability of the simulation.